Reversed North Atlantic gyre dynamics in present and glacial climates

Marisa Montoya · Andreas Born · Anders Levermann

Abstract The dynamics of the North Atlantic subpolar gyre (SPG) are assessed under present and glacial boundary conditions by investigating the SPG sensitivity to surface wind-stress changes in a coupled climate model. To this end, the gyre transport is decomposed in Ekman, thermohaline, and bottom transports. Surface wind-stress variations are found to play an important indirect role in SPG dynamics through their effect on water-mass densities. Our results suggest the existence of two dynamically distinct regimes of the SPG, depending on the absence or presence of deep water formation (DWF) in the Nordic Seas and a vigorous Greenland–Scotland ridge (GSR) overflow. In the first regime, the GSR overflow is weak and the SPG strength increases with wind-stress as a result of enhanced outcropping of isopycnals in the centre of the SPG. As soon as a vigorous GSR overflow is established, its associated positive density anomalies on the southern GSR slope reduce the SPG strength. This has implications for past glacial abrupt climate changes, insofar as these can be explained through latitudinal shifts in North Atlantic DWF sites and strengthening of the North Atlantic current. Regardless of the ultimate trigger, an abrupt shift of DWF into the Nordic Seas could result both in a drastic reduction of the SPG strength and a sudden reversal in its sensitivity to wind-stress variations. Our results could provide insight into changes in the horizontal ocean circulation during abrupt glacial climate changes, which have been largely neglected up to now in model studies.

M. Montoya (✉)
Dpto. Astrofísica y Ciencias de la Atmósfera,
Facultad de Ciencias Físicas, Universidad Complutense de
Madrid, Ciudad Universitaria, Madrid, Spain
e-mail: mmontoya@fis.ucm.es

A. Born
Bjerknes Centre for Climate Research, Bergen, Norway

A. Born
Geophysical Institute, University of Bergen, Bergen, Norway

A. Levermann
Earth System Analysis, Potsdam Institute for Climate Impact
Research, Potsdam, Germany

A. Levermann
Institute of Physics, Potsdam University, Potsdam, Germany

1 Introduction

The North Atlantic subpolar gyre (SPG) is an important component of the global ocean circulation and plays a crucial role in climate variability (Treguier et al. 2005). Its dynamics have received renewed attention in the last years, since a decline in its strength in the nineties as observed from satellite altimeter data was associated with a reduction in the Atlantic meridional overturning circulation (AMOC) (Häkkinen and Rhines 2004). Through its modulation of the North Atlantic Current, the SPG has been found to exert a strong control on the surface salinity of the northeastern North Atlantic on interannual to interdecadal timescales, suggesting that the recent high salinities recorded in this region have been a consequence of the former SPG strength decline (Hátún et al. 2005). This decline has subsequently been found to reflect decadal variability, rather than a long term trend (Böning et al. 2006). The former mechanism has recently been found to

operate also at millennial timescales throughout the Holocene (Thornalley et al. 2009). Although far from being well understood, the relationship between the SPG and the AMOC suggests the potential of SPG changes to monitor AMOC changes (Böning et al. 2006; Häkkinen and Rhines 2004; Zhang 2008).

While surface wind-stress has large influence on its strength and variability (Böning et al. 2006; Curry et al. 1998), the SPG circulation is also partly controlled by baroclinic adjustments and therefore by the density structure in the subpolar North Atlantic (Eden and Willebrand 2001; Greatbatch et al. 1991; Mellor et al. 1982; Myers et al. 1996; Penduff et al. 2000). This has shown to have two important consequences for its dynamics. Firstly, model results have recently suggested the existence of at least two stable SPG states as a consequence of positive feedbacks involving the transport of temperature and salinity toward the centre of the gyre and the interaction with the Greenland-Scotland ridge (GSR) overflow (Levermann and Born 2007). In addition, the SPG strength has proved to be strongly sensitive to deep convection (Born et al. 2009b; Treguier et al. 2005). Recently, improving the representation of water masses in the Nordic Seas and the subpolar North Atlantic has shown to result in a substantial strengthening of the SPG in climate simulations (Born et al. 2009a).

Despite these recent efforts, a complete understanding of the SPG dynamics remains elusive. Here we address this issue by analysing quantitatively the sensitivity of the SPG to the surface wind-stress in idealised climate simulations both under present and glacial boundary conditions. Surface wind-stress variations are found to play an indirect role in the SPG dynamics through their effect on water-mass densities, while the existence of a GSR overflow appears to have a dramatic impact on the SPG strength as well as on its dynamics.

The paper is organised as follows: in Sect. 2 the model and experimental setup are described. In Sect. 3 the SPG strength response to wind-stress changes is investigated by analysing the components of the vertically integrated momentum equations (Ekman, thermohaline, and bottom transports), and the impact of surface wind-stress changes on the SPG strength through changes in the water-mass densities is described. Finally, in Sect. 4 the main conclusions are summarised.

2 Model and experimental setup

The model used in this study is the CLIMBER-3α coupled climate model (Montoya et al. 2005). Its atmospheric component is a statistical-dynamical model (Petoukhov et al. 2000). The oceanic component contains the GFDL

MOM-3 ocean general circulation model, with a horizontal resolution of 3.75° and 24 vertical levels, and the ISIS thermodynamic-dynamic snow and sea-ice model (Fichefet and Maqueda 1997). The version used herein includes a few modifications with respect to the standard configuration described by Montoya et al. (2005) in order to improve the model's performance for preindustrial climate: isopycnal diffusivity was doubled to $\kappa_h = 2{,}000$ m^2 s^{-1} and bathymetry amids the Indonesian islands was slightly deepened. As a consequence, the Indonesian throughflow increased from about 7 Sv (1 Sv = 10^6 m^3 s^{-1}) in the previous version to 10 Sv, which is in the range of observations for present-day climate (Wijffels et al. 2008), the surface salinity distribution and the stratification in the deep ocean improved (not shown), and the strength of the AMOC increased from about 12 to 17 Sv, comparable to current estimates (Ganachaud and Wunsch 2000; Talley et al. 2003).

Climate simulations were performed both for present (preindustrial) and glacial boundary conditions (Montoya and Levermann 2008). Preindustrial boundary conditions consist of the present-day Earth geography and ice-sheet distribution, vegetation (disregarding land-use changes due to human activities), insolation, and atmospheric CO$_2$ concentration (280 ppmv), as described by Montoya et al. (2005). For glacial boundary conditions, the PMIP2 specifications (http://pmip2.lsce.ipsl.fr) for the Last Glacial Maximum (LGM, ca. 21,000 years before present) were imposed, namely: changes in insolation, a reduced equivalent atmospheric CO$_2$ concentration of 167 ppmv to account for the lowered CH$_4$, N$_2$O, and CO$_2$ concentrations, the ICE-5G ice-sheet reconstruction (Peltier 2004), and land-sea mask changes plus a global increase of salinity by 1 psu to account for the ~ 120 m sea-level lowering. Oceanic bathymetry, vegetation, and river-runoff routing were unchanged with respect to the Holocene simulation.

An important issue when assessing the glacial ocean circulation is the fact that glacial winds are poorly constrained at present. This issue is critical, since surface winds force the ocean circulation both directly and indirectly, by enhancing vertical mixing and altering the density structure (Kuhlbrodt et al. 2007; Toggweiler and Samuels 1998; Wunsch 1998; Wunsch and Ferrari 2004). Stronger glacial meridional surface temperature gradients and evidence mainly from ice-core data for greatly increased dust and sea-salt concentrations have led to the general assumption of considerably stronger than present surface winds, possibly by more than 50% (Crowley and North 1991 and references therein). However, enhanced aerosol concentrations also reflect changes in the sources such as enhanced aridity. Models furthermore show enhanced westerlies but not uniformly enhanced surface

winds (e.g. Hewitt et al. 2003; Otto-Bliesner et al. 2006). Recently, it has been claimed that, because westerly winds respond mainly to changes in the thermal contrast in the mid-atmosphere rather than to changes at the surface, and because the mid-atmosphere thermal contrast increases with the atmospheric CO_2 concentration, lower than present glacial CO_2 atmospheric levels should have led to weaker than present glacial westerly winds (Toggweiler and Russell 2008).

In order to take this uncertainty into account, Montoya and Levermann (2008) integrated the model to equilibrium with the Trenberth et al. (1989) surface wind-stress climatology multiplied globally by varying factors $\alpha \in [0.5, 2]$ (hereafter, LGMα). To assess the potential of multiple stable states, two different initial conditions were used: equilibrium simulations with either $\alpha = 1$ (LGM1.0) or $\alpha = 2$ (LGM2.0). The resulting LGM equilibrium simulations for a given α value are denoted LGMα-weak and LGMα-strong. The simulated glacial AMOC strength was found to increase continuously with surface wind-stress up to $\alpha_c \equiv 1.7$ (Fig. 1a, see also Montoya and Levermann (2008)). For $\alpha \lesssim \alpha_c \equiv 1.7$, deep water formation (DWF) takes place south of the GSR. At $\alpha = \alpha_c \equiv 1.7$ a threshold is found, associated with a drastic AMOC increase of more than 10 Sv, a northward shift of DWF north of the GSR, and a strengthening of the GSR overflow (Fig. 1b). In the vicinity of this threshold ($\alpha \simeq 1.7 - 1.75$) the AMOC exhibits two stable states, with weak and strong circulation, respectively.

To assess whether this behaviour is unique to the LGM, similar simulations with varying surface wind-stress were carried out for the Holocene (hereafter, HOLOα). Note since in these DWF in the Nordic Seas already takes place for $\alpha = 1$ (Fig. 1b), only reduced wind-stress with $\alpha \in [0.25, 1]$ was considered. In this case, contrarily to the LGM, the overflow increases continuously with wind-stress (Fig. 1b) and the AMOC strength increase with wind-stress is roughly linear (Fig. 1a).

The dynamical mechanism behind the non-linear behaviour found in the LGM runs is based on an altered salinity distribution in the North Atlantic. Enhanced surface wind-stress increases the horizontal gyre circulation both in the subtropics and the subpolar region. As a consequence, more salt is transported from the tropics to the North Atlantic in the upper ocean layers. Higher subtropical sea surface temperatures (SSTs) also result in enhanced evaporation and thereby higher subtropical surface salinities, but the relevant mechanism at high northern latitudes is the increased salt transport (Montoya and Levermann 2008). For $\alpha \leq \alpha_c$ the AMOC increase is thus gradual in response to a gradual increase in gyre salinity transport. In this regime, deep convection and DWF are confined to the region south of the Greenland–
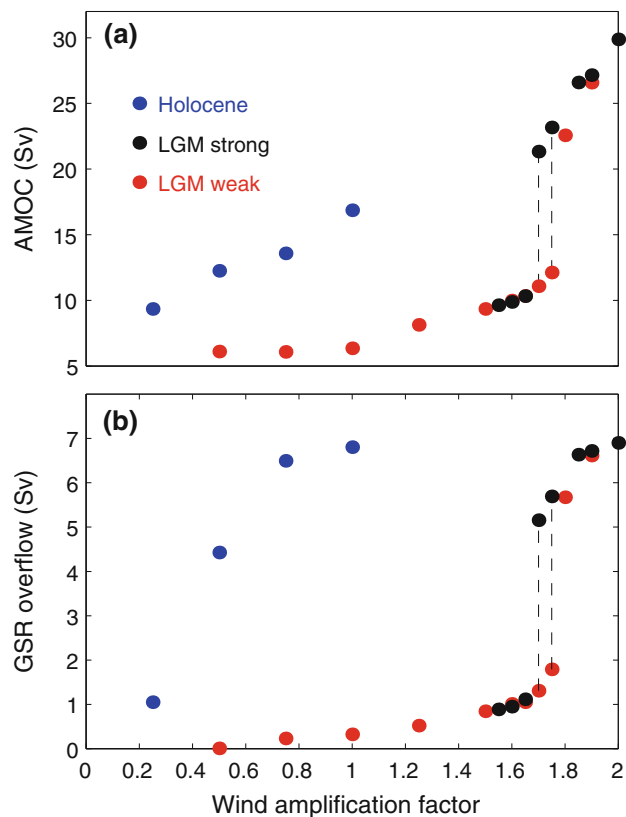

Fig. 1 a AMOC strength (see also Montoya and Levermann 2008) and **b** GSR overflow as a function of wind-stress enhancement factor α for the LGM (*black, red*) and Holocene (*blue*), in Sv. *Black* and *red dots* indicate LGM equilibrium simulations starting from LGM2.0 (LGMα-strong) and LGM1.0 (LGMα-weak), respectively. The glacial AMOC strength increases continuously with surface wind-stress up to $\alpha_c \equiv 1.7$. For $\alpha \leq \alpha_c$, DWF takes place south of the GSR. At $\alpha = \alpha_c$ a threshold is found associated with a drastic AMOC increase of more than 10 Sv, a northward shift of DWF north of the GSR, and a strengthening of the GSR overflow. In the vicinity of this threshold ($\alpha \simeq 1.7$) the AMOC exhibits two stable states, with weak and strong circulation, respectively. The Holocene, in contrast, shows a roughly linear increase of the AMOC strength with wind-stress in response to the more gradual GSR overflow increase

Scotland ridge. For $\alpha > \alpha_c$ the gyre salinity transport to the Nordic Seas is sufficient to induce DWF there and strengthen the AMOC. The enhanced overturning triggers a positive salt-advection feedback (Rahmstorf 1996). More salt is transported from the south toward high northern latitudes by the AMOC and, consequently, salinity increases in the Nordic Seas and the overturning further strengthens.

These results show the GSR overflow and AMOC exhibit very different sensitivities to surface wind-stress changes in the LGM and HOLO runs. As mentioned previously (Sect. 1), baroclinic adjustments following changes in the GSR overflow have been shown to play a very important role in SPG dynamics (Born et al. 2009a; Levermann and Born 2007). Herein, the sensitivity of the

SPG strength to surface wind-stress is investigated in the aforementioned runs.

3 Results

3.1 SPG strength variation with surface wind-stress

Due to its explicit free surface the ocean model used herein does not have a well defined vertically integrated (barotropic) streamfunction. Born et al (2009a) thus calculated the SPG strength by integrating the vertically integrated zonal transport M_x meridionally between the southern Greenland coast and the SPG centre (hereafter $\overline{M}_x$), which in turn is defined so that the former integral is maximum.

Using the same procedure, $\overline{M}_x$ is found to increase monotonically with increasing surface wind-stress in the LGM runs, while it does not show a clear behaviour in the HOLO runs (Fig. 2). Nevertheless, changes in AMOC strength and GSR overflow in response to wind-stress variations impact strongly on the flow path in the subpolar North Atlantic, most notably in the LGM runs. This is illustrated by analysing the water-mass flow in the subpolar North Atlantic without and with a strong GSR overflow (Fig. 3). Without a strong GSR overflow most of the sinking takes place at the southern rim of the SPG, south of 40°N, and the upper ocean provides the bulk of the SPG
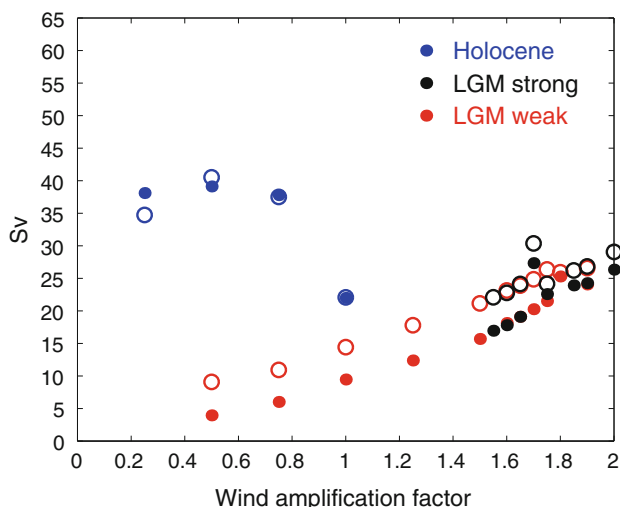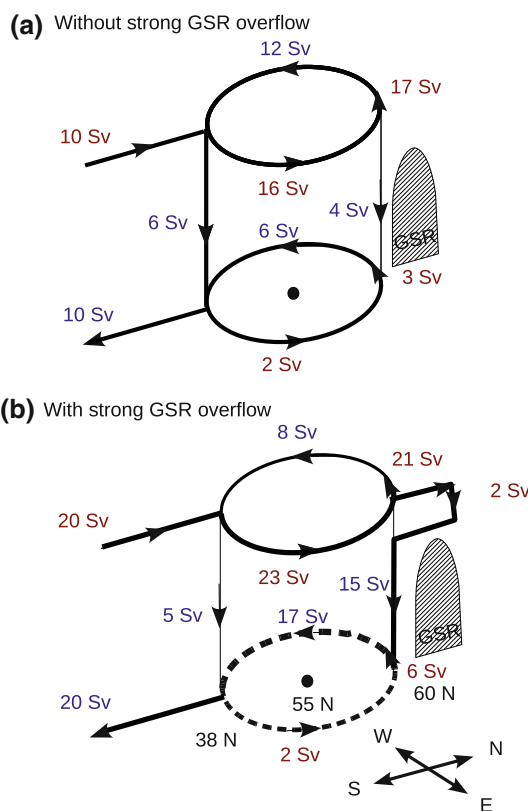

Fig. 3 Schematic figure indicating the flow of water masses in the subpolar North Atlantic **a** in LGM1.7-weak, without a strong GSR overflow, and **b** in LGM1.7-strong, with a strong GSR overflow. The main flow paths are represented by *thick lines* with *arrows*. The *upper* and *lower branches* represent the flows integrated vertically in the upper 1,000 m and in the deep ocean as well as zonally, east and west of the SPG centre (located at ca. 34°W and 55°N), at different latitudes: 38°N, the SPG centre (ca. 55°N), and 60°N. Eastward and northward flows are represented in *red*, while westward and southward flows are in *blue* (see text for a more detailed explanation)

flow. As an example, in LGM1.7-weak $\overline{M}_x$ is ca. 20 Sv. Of these, about 17 and 3 Sv flow westward within and below the upper 1,000 m, respectively (Fig. 3a). A similar amount (18 Sv) is obtained when integrating the meridional, vertically integrated transport M_y zonally between the coast of North America and the SPG centre (hereafter $\overline{M}_y$). Of these, about 12 and 6 Sv flow southward in the upper 1,000 m and in the deep ocean, respectively. In LGM1.7-strong, which shows a vigorous GSR overflow (Fig. 3b), the upper AMOC inflow is strongly intensified. Most of this water circulates in the eastern section of the North Atlantic (northward branch of SPG), sinks in the Nordic Seas and flows south in the western branch of the SPG. The total southward transport increases up to ca. 25 Sv, but only 8 Sv take place in the upper 1,000 m while about 17 Sv flow south in the deep ocean. Thus, the upper southward and deep northward flows are strongly diminished.

Fig. 2 Magnitude of the zonal transport $\overline{M}_x$ between the southern Greenland coast and the centre of the SPG, integrated vertically within the whole water column, as a function of wind-stress enhancement factor α for the LGM (*black*, *red*) and Holocene (*blue*), in Sv (*closed circles*). *Black* and *red dots* indicate LGM equilibrium simulations starting from LGM2.0 (LGMα-strong) and LGM1.0 (LGMα-weak), respectively. Also shown is the sum of the three terms in the r.h.s. of Eqs. 1 and 4–6 for M_x shown in Fig. 4b–d (*open circles*)

As the GSR overflow and the AMOC strengthen with wind-stress, the upper northward flow is intensified mainly in the northeastern North Atlantic, reflecting a strengthening of the North Atlantic Current. North Atlantic Deep Water (NADW) formation increases, and its southward flow is enhanced mainly along the deep western boundary, while the recirculation toward the basin interior is strongly diminished (Fig. 3b). Accordingly, variations in the total horizontal transport around the SPG centre reflect to a large extent AMOC changes. To isolate exclusively the flow which recirculates within the subpolar North Atlantic in the whole water column, AMOC variations must be subtracted. Thus, the SPG strength is estimated as the difference between $\overline{M}_x$ and the maximum AMOC strength at the latitude of the SPG centre. The idea behind this is that in the extreme case in which the upper flow is northward at all longitudes and returns southward along the western boundary current we cannot truly speak of a gyre. Instead the circulation is fully represented by the AMOC. Note as long as changes in the AMOC strength are not very large the usual definition of the SPG strength is fully appropriate, and the SPG strength variations are consistent with those used herein (e.g. Born et al. 2009a; Levermann and Born 2007).

For any given value of the wind-stress, the SPG is found to be considerably stronger in the Holocene than in the LGM (Fig. 4a). In addition, it shows a qualitatively different sensitivity to surface wind-stress under each of these climatic conditions. In the Holocene it generally decreases with increasing wind-stress. In the LGM, for

$\alpha < 1.7$, it increases roughly linearly with wind-stress extrapolating to zero for $\alpha = 0$, only decreasing abruptly once the GSR overflow is initiated for $\alpha > 1.7$. Thus, a threshold is found in the SPG strength at the same value as in the AMOC and the GSR overflow (see Fig. 1 and Montoya and Levermann 2008). Note that the SPG strength in the LGM runs vanishes for high α values, reflecting the fact that, as mentioned above, the upper and deep circulation are northward and southward, respectively, practically everywhere and thus the circulation is well represented by the AMOC.
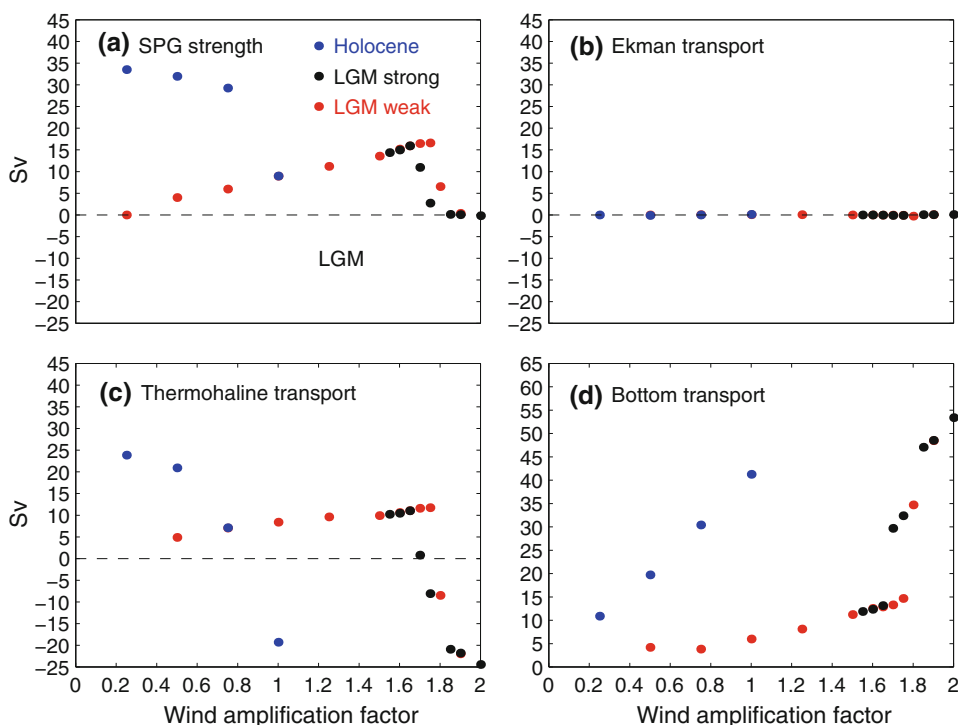
3.2 Flow decomposition

In order to gain further insight into the former behaviour, the contributions to the SPG strength are analysed (see e.g. Born et al. 2009a; Mellor et al. 1982). Ignoring frictional terms, the vertically integrated zonal and meridional time-independent transports are given by (see Appendix):

$$fM_x = -Hg\partial_y\eta + H\int_{-H}^{0}\partial_y b dz + \int_{-H}^{0}z\partial_y b dz + \rho_0^{-1}\tau_{0y} \quad (1)$$

$$fM_y = Hg\partial_x\eta - H\int_{-H}^{0}\partial_x b dz - \int_{-H}^{0}z\partial_x b dz - \rho_0^{-1}\tau_{0x} \quad (2)$$

where M_x and M_y are the zonal and meridional vertically integrated transports, respectively, f is the Coriolis parameter, H the ocean depth, g local gravity, η the sea-

Fig. 4 Relevant components of North Atlantic volume transport as a function of wind-stress enhancement factor α for the LGM (*black, red*) and Holocene (*blue*): **a** SPG strength, **b** Ekman transport, **c** thermohaline transport, and **d** bottom transport contributions to the SPG strength as in Eqs. 1 and 4–6 for M_x. Note here the magnitudes of the former terms are represented. *Black* and *red dots* indicate LGM equilibrium simulations starting from LGM2.0 (LGMα-strong) and LGM1.0 (LGMα-weak), respectively (in Sv)

surface elevation, ρ_0 the average density, τ_{0x} and τ_{0y} the surface wind stresses, and

$$b = g \frac{\rho_0 - \rho}{\rho_0} \tag{3}$$

the buoyancy. Identification of the Ekman, thermohaline, and bottom velocities as defined by Fofonoff (1962) (see also Mellor et al. 1982) allows decomposing Eqs. 1 and 2 into their respective vertically integrated Ekman, thermohaline and bottom transports:

$$f[M_{xe}, M_{ye}] = [\rho_0^{-1}\tau_{0y}, -\rho_0^{-1}\tau_{0x}] \tag{4}$$

$$f[M_{xt}, M_{yt}] = \left[\int_{-H}^{0} z\partial_y b\,dz, - \int_{-H}^{0} z\partial_x b\,dz \right] \tag{5}$$

$$f[M_{xb}, M_{yb}]$$
$$= \left[-Hg\partial_y\eta + H\int_{-H}^{0} \partial_y b\,dz, Hg\partial_x\eta - H\int_{-H}^{0} \partial_x b\,dz \right]. \tag{6}$$

As explained in Sect. 3.1, the SPG strength (Fig. 4a) is calculated by subtracting the AMOC strength from the integral of M_x from the coast of Greenland to the SPG centre ($\overline{M}_x$). The corresponding integrals of the r.h.s. terms in Eq. 1 are shown in Fig. 4b–d. The direct contribution of the wind-stress through the Ekman transport is found to be negligible (Fig. 4b), in agreement with Mellor et al. (1982). This result might seem trivial given that, according to Sverdrup balance, the curl of the surface wind-stress rather than its local value drives the overall gyre transport. However, high-resolution models indicate that the SPG does not obey simple Sverdrup dynamics (Bryan et al. 1995; Treguier et al. 2005). The SPG strength (Fig. 4a) instead closely follows the variation of the thermohaline transport (Fig. 4c). Without overflow (LGM runs for $\alpha < \alpha_c \equiv 1.7$) the thermohaline transport and the SPG strength slowly increase with increasing α. Once a relatively strong overflow sets in (HOLO runs and LGM runs for $\alpha > \alpha_c \equiv 1.7$), both decrease abruptly with increasing α. The bottom transport (Fig. 4d) instead follows the variations in the AMOC and GSR overflow (Fig. 1), increasing monotonically with α both under present and glacial boundary conditions, and showing a threshold at $\alpha = \alpha_c \equiv 1.7$ above which their sensitivity to wind-stress variations increases considerably. The dynamics underlying the SPG and the AMOC are thus very different, supporting their conceptual distinction. Finally, note the sum of the (meridionally integrated) Ekman, thermohaline and bottom transports on the r.h.s. of Eq. 1 gives roughly the same result as the vertically integrated zonal transport $\overline{M}_x$ on the l.h.s. (Fig. 2, open and closed circles, respectively).

The existence of a GSR overflow thus clearly determines the effect of wind-stress changes on the SPG strength and AMOC through its effect on the thermohaline and bottom transport. We can distinguish two regimes, one with suppressed GSR overflow, corresponding to the LGM runs for $\alpha < \alpha_c \equiv 1.7$, and one with active GSR overflow, corresponding to the Holocene runs and the LGM runs for $\alpha > \alpha_c \equiv 1.7$. Without overflow the thermohaline transport slowly increases with α, leading to an increase in SPG strength. The same applies to the bottom transport. Once a relatively strong overflow sets in, the thermohaline transport, and thus the SPG strength, decreases abruptly with increasing α, while the bottom transport increase with α proceeds faster.

3.3 Wind-induced density changes

In order to assess how wind-stress changes affect the thermohaline transport and thus the SPG strength within each regime, that is, with and without a strong overflow, the meridional density gradient weighted by depth ($z \cdot \partial_y \rho$), which constitutes the core of the thermohaline transport (Eq. 1), is considered in the subpolar North Atlantic. Figure 5 shows its zonal average over the SPG centre (40°W–20°W) for several of the former experiments. Superimposed are the contours of the isopycnals, averaged zonally in the same region, whose slope is indicative of the SPG strength.

Increasing the wind-stress from LGM1.0 to LGM1.7-weak leads to enhanced northward salt transport as well as upwelling and outcropping of isopycnals in the centre of the SPG in LGM1.7-weak relative to LGM1.0 (Fig. 5a, b), and thereby a more efficient mixing of heat to depth and out of the SPG centre. This leads to cooling (Fig. 6), an increase in density in the SPG centre (Fig. 5c), and thereby to a stronger gyre (Eq. 1). This mechanism points to the positive feedback between temperature and the SPG strength (Levermann and Born 2007). North (south) of the SPG centre, the meridional density gradient weighted by depth ($z \cdot \partial_y \rho$) is negative (positive), indicating westward and eastward flow north and south of the SPG centre, respectively (Fig. 5c).

In LGM1.7-strong, DWF in the Nordic Seas is enhanced relative to LGM1.7-weak (Fig. 5d–f). The enhanced overflow thus translates into a density increase mainly south of the GSR. This results in a positive anomalous meridional density gradient and thus eastward anomalous circulation in this area, explaining the SPG strength reduction with increasing wind-stress. Thus, density changes associated with the overflow on the southern GSR slope play a major role in the SPG strength reduction once the second regime is entered.

Fig. 5 Meridional density gradient weighted by depth ($z \cdot \partial_y \rho$), averaged over the SPG centre (40°W–20°W), for **a** LGM1.0, **b** LGM1.7-weak, and **c** LGM1.7-weak minus LGM1.0; **d–f** same fields for LGM1.7-weak, LGM1.7-strong, and LGM1.7-strong minus LGM1.7-weak, in 10^{-4} kg m^{-3}. Note here $0 \leq z \leq H$. Thus positive anomalies correspond to positive values in the core of the thermohaline term (Eqs. 1 and 5). Superimposed contours show the corresponding isopycnals (*black*, in 10^{-4} kg m^{-3})
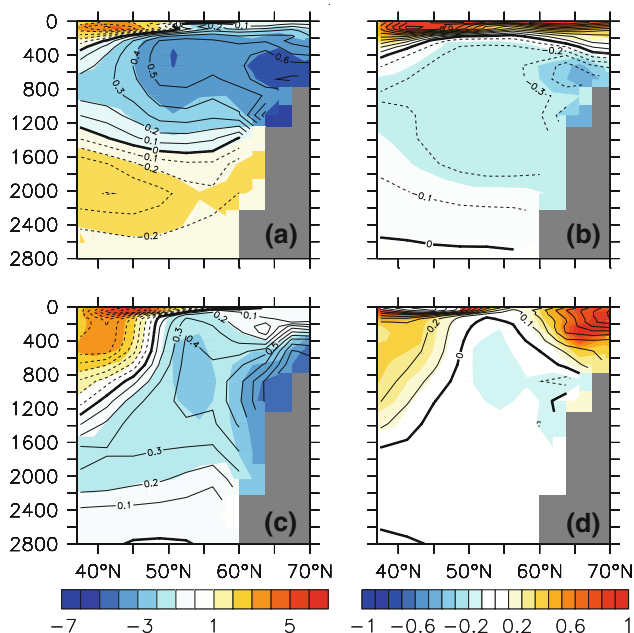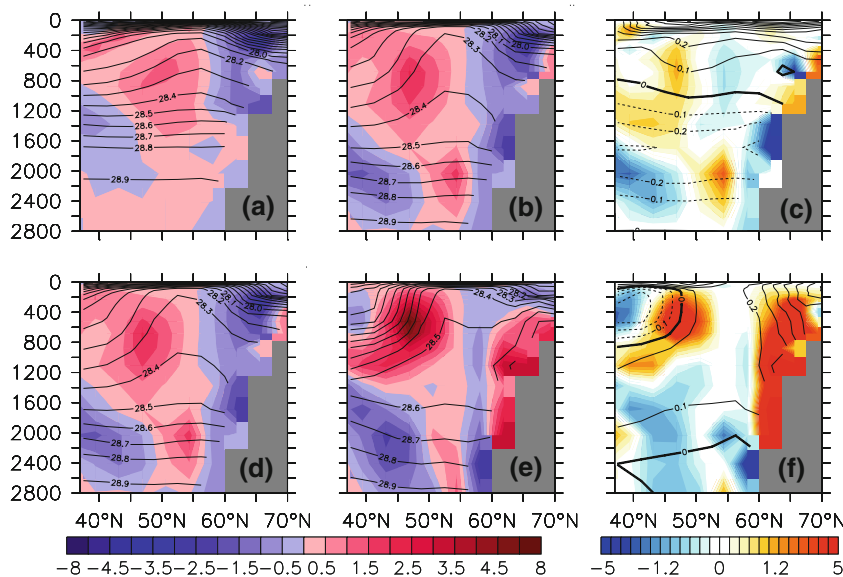

Fig. 6 Difference between LGM1.7-weak and LGM1.0 (LGM1.7-weak minus LGM1.0) **a** temperature (in K) and **b** salinity (in psu) averaged over the SPG centre (40°W–20°W); **c, d** same fields for LGM1.7-strong minus LGM1.7-weak. Superimposed contours show the corresponding contributions of temperature and salinity changes to density changes shown in contours in Fig. 5c, f

The latter mechanism explains as well the decrease in the SPG strength with increasing α in the the HOLO runs (Fig. 4a). Note that this decrease is fastest from $\alpha = 0.75$ to $\alpha = 1$, which yields the low SPG strength value for present-day winds (HOLO1.0). This might seem contradictory with the fact that the GSR overflow increase actually proceeds more slowly for $\alpha \geq 0.75$. Yet, the SPG strength goes in parallel with the decrease in the

thermohaline transport (Fig. 4c). Comparison of the $z \cdot \partial_y \rho$ anomaly for HOLO0.75 relative to HOLO0.5 (Fig. 7c) and HOLO1.0 relative to HOLO0.75 (Fig. 7f) reveals density changes along the southern GSR slope result in a stronger SPG reduction in the latter case. A further decomposition of these density changes into temperature and salinity shows these are mainly caused by colder North Atlantic temperatures being entrained by the overflow along the GSR slope (Fig. 8c; note that temperature anomalies along the GSR slope are larger than in Fig. 8a). This implies that not only the magnitude of the overflow, but also the water-mass characteristics are important in setting the SPG circulation response.

To summarise, in the absence of a strong overflow, a wind-stress increase results in a reduction of the upper ocean temperature as a consequence of enhanced outcropping of isopycnals. The latter leads to a density increase in the SPG centre relative to its rim, and thus to a stronger SPG (Fig. 9). In the presence of a significant GSR overflow, wind stress enhances downward transport of cold water masses into GSR slope water, which reduces the density gradient across the SPG and thereby its strength. As a result, the sensitivity to wind-stress in glacial and interglacial times is opposite.

4 Conclusions and discussion

We have investigated the sensitivity of the SPG strength to wind-stress changes under present and glacial climates. Two regimes can be distinguished, depending on the existence of a vigorous GSR overflow. In the first one, GSR overflow is weak and the SPG strength increases with wind-stress as a result of enhanced outcropping of

Fig. 7 As Fig. 5 but for **a**
HOLO0.5, **b** HOLO0.75, and **c**
HOLO0.75 minus HOLO0.5; **d**–
f same fields for HOLO0.75,
HOLO1.0, and HOLO1.0 minus
HOLO0.75, in 10^{-4} kg m^{-3}.
Superimposed contours show
the corresponding isopycnals
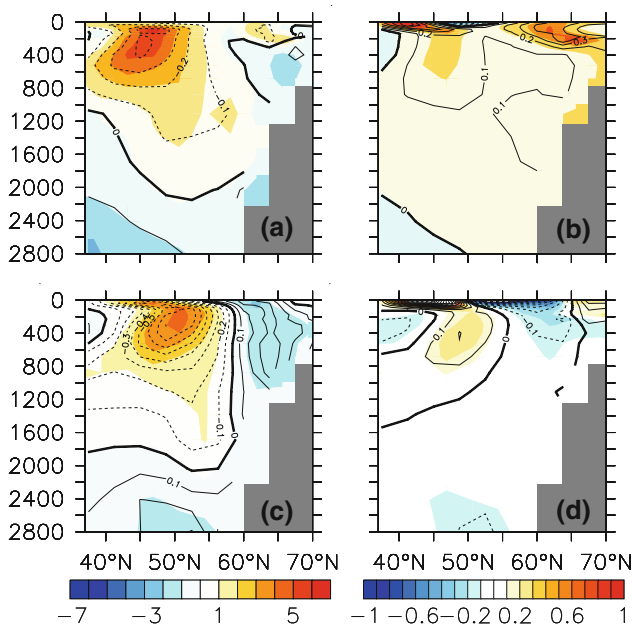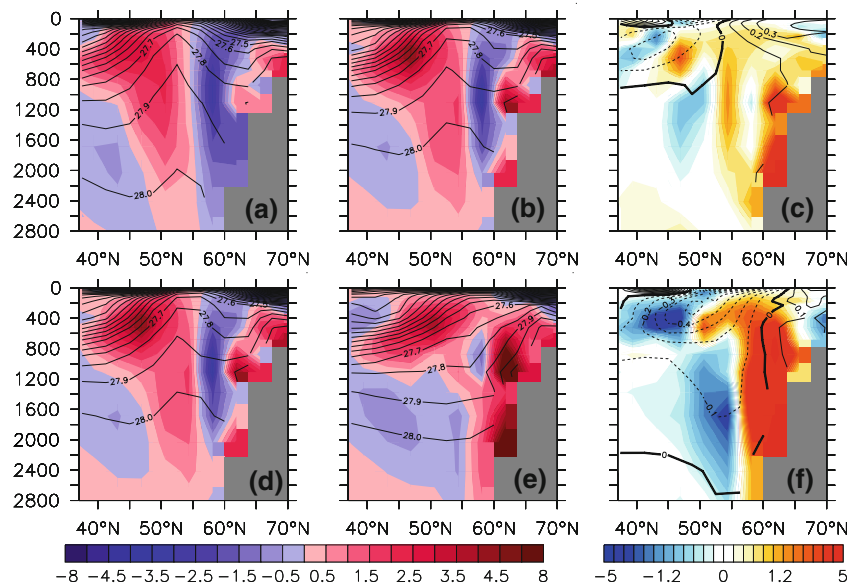(*black*, in 10^{-4} kg m^{-3})

Fig. 8 As Fig. 6 but for HOLO0.75 minus HOLO0.5 (**a, b**) and
HOLO1.0 minus HOLO0.75 (**c, d**). Superimposed contours show the
corresponding contributions of temperature and salinity changes to
density changes shown in contours in Fig. 7c, f

Fig. 9 Mechanisms describing how a wind-stress increase affects the
SPG strength through its effect on North Atlantic water-mass
densities with and without a strong overflow over the GSR. *Signs
between ellipses* indicate how a given magnitude responds to
variations in the previous one within the schematic. Without a strong
overflow (*red*), a wind-stress increase results in enhanced outcropping
of isopycnals in the SPG centre and thus cooling there. This leads to a
density increase in the centre of the SPG and thus to a stronger SPG.
In the presence of an overflow (*blue*), wind-stress enhances downward
transport of cold water masses into GSR slope water which reduces
the density gradient across the SPG and thereby its strength

isopycnals. As soon as DWF in the Nordic Seas and a
vigorous GSR overflow are established, positive density
anomalies on the southern slope of the GSR resulting from
the overflow reduce the SPG strength. This reduction is
abrupt in the LGM in response to the abrupt onset of DWF,
and smooth in the Holocene following the more gradual
GSR overflow increase there.

This study was motivated by two previous results. First,
Montoya and Levermann (2008) found a threshold in the
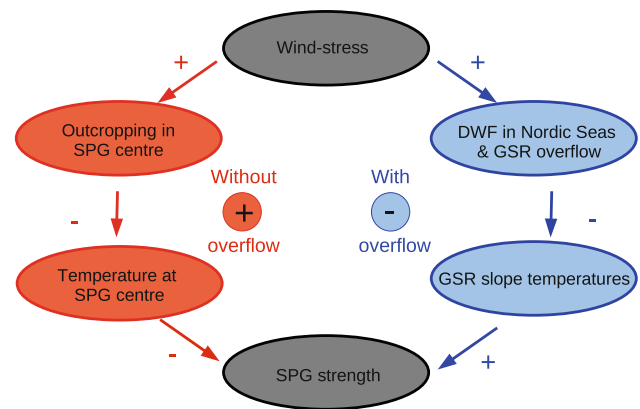AMOC as well as in the GSR overflow with respect to

wind-stress in glacial climate simulations. Second, Born
et al. (2009a) analysed the impact of the representation of
the overflows over the GSR in coarse resolution models.
Using a hydraulic flow parametrisation, they found that an
improved representation of water masses in the Nordic
Seas and the subpolar North Atlantic resulted in a stronger
SPG. By contrast, an artificial deepening of the topography
resulted in a weaker SPG as a result of its stronger GSR
overflow and associated water masses. Taken together,
these two studies prompted us to analyse the behaviour of
the SPG in the aforementioned runs. Our results thus fully

agree with the finding of Born et al. (2009a) indicating that the GSR overflow interacts strongly with the SPG, and that a stronger GSR overflow leads to a weaker SPG, but furthermore indicate the existence of two dynamical regimes, depending on the existence of DWF in the Nordic Seas and a vigorous GSR overflow. Note that AMOC variations are small in the study by Born et al. (2009a) and thus not corrected for in the SPG definition. The generalisation presented here is thus fully consistent.

It is conceivable that our results could be affected by the model's specific configuration, deficiencies, and resolution. An imperfect representation of water masses in the North Atlantic and interaction with the boundaries in the presence of the high viscosity required in such coarse resolution models are likely to impact the SPG circulation. Indeed, the present-day SPG in our model is too weak, and deep convection is shifted from the Labrador Sea to the Irminger Sea. As a consequence, the SPG does not enter Labrador Sea. However, the large-scale circulation under concern in this study is simulated consistently: convection occurs inside the SPG and a cyclonic rim current embraces the deep convection area. The central issue here is the existence of different regimes in the absence and presence of a strong GSR overflow. The governing mechanisms in each of these regimes are simple enough and well understood. Thus, we are confident that the main conclusions presented here are robust and not severely affected by the former features.

Our experimental setup, consisting in multiplying the wind-stress by a constant factor, is highly idealised. Changes in the surface wind-patterns should be the focus of future work. However, our main result is the existence of different dynamical regimes depending on the presence or absence of deep water formation north of the GSR and a vigorous overflow, and the role of wind-stress changes here is merely to trigger the latter. We thus expect our results to be robust against more realistic forcings.

Our findings might be helpful in understanding paleoclimatic records. Abrupt climatic changes of the last glacial period, so called Dansgaard–Oeschger events, have been explained through latitudinal shifts in North Atlantic DWF sites and strengthening of the North Atlantic current (Ganopolski and Rahmstorf 2001; Rahmstorf 2002). While interstadials are associated with DWF in the Nordic Seas and the existence of an overflow over the GSR, during stadials DWF takes place south of the GSR with no overflow. Thus, reversed SPG strength sensitivities to wind forcing are expected in each of these phases. Regardless of their ultimate trigger, glacial abrupt climate changes could result both in a drastic reduction of the SPG strength and a sudden change in its sensitivity to wind-stress variations. SPG dynamics have recently been found to play an important role throughout the Holocene by driving

millennial variability in the Atlantic inflow to the Nordic Seas (Thornalley et al. 2009). Our results furthermore imply they could play a relevant role in past glacial abrupt climate changes.

Model studies on glacial abrupt climate changes have up to now mainly focused on the AMOC, largely neglecting changes the horizontal circulations, such as those associated with the gyres. Our study could provide insight as to how the latter might have been affected during such abrupt changes, and may be tested through comparison against paleodata.

Appendix

Ignoring frictional terms, the zonal and meridional time-independent momentum equations are:

$$fu = -g\partial_y\eta + \partial_y \int_z^0 b'dz' + \rho_0^{-1}\partial_z\tau_{zy} \tag{A1}$$

$$-fv = -g\partial_x\eta + \partial_x \int_z^0 b'dz' + \rho_0^{-1}\partial_z\tau_{zx}, \tag{A2}$$

with u and v being the zonal and meridional velocity components, f the Coriolis parameter, g local gravity, η the sea-surface elevation, ρ_0 the average density, τ_{zx} and τ_{zy} the turbulent Reynolds stresses, and

$$b = g\frac{\rho_0 - \rho}{\rho_0} \tag{A3}$$

the buoyancy.

Splitting the second term on the right hand side (r.h.s.) of Eqs. A1 and A2 we have:

$$fu = -g\partial_y\eta + \partial_y \int_{-H}^0 bdz - \partial_y \int_{-H}^z b'dz' + \rho_0^{-1}\partial_z\tau_{zy} \tag{A4}$$

$$-fv = -g\partial_x\eta + \partial_x \int_{-H}^0 bdz - \partial_x \int_{-H}^z b'dz' + \rho_0^{-1}\partial_z\tau_{zx}, \tag{A5}$$

where H is the ocean depth.

Here we can identify the Ekman, thermohaline and bottom velocity as defined by Fofonoff (1962) and Mellor et al. (1982):

$$f[u_e, v_e] = \left[\rho_0^{-1}\partial_z\tau_{zy}, -\rho_0^{-1}\partial_z\tau_{zx}\right] \tag{A6}$$

$$f[u_t, v_t] = \left[-\partial_y \int_{-H}^z b'dz', \partial_x \int_{-H}^z b'dz'\right] \tag{A7}$$

$$f[u_b, v_b] = \left[-g\partial_y\eta + \partial_y \int_{-H}^{0} b\,dz, g\partial_x\eta - \partial_x \int_{-H}^{0} b\,dz \right]. \quad (A8)$$

We now define the vertically integrated zonal and meridional transports:

$$M_x = \int_{-H}^{0} u\,dz; \quad M_y = \int_{-H}^{0} v\,dz. \quad (A9)$$

Integrating vertically Eq. A4 we have:

$$fM_x = -g \int_{-H}^{0} \partial_y\eta\,dz + \int_{-H}^{0} dz\partial_y \int_{-H}^{0} b\,dz$$
$$- \int_{-H}^{0} dz\partial_y \int_{-H}^{z} b'\,dz' + \rho_0^{-1} \int_{-H}^{0} \partial_z\tau_{zy}\,dz. \quad (A10)$$

The third term on the r.h.s. can be rewritten as follows using Leibnitz's rule:

$$\int_{-H}^{0} dz\partial_y \int_{-H}^{z} b'\,dz' = \partial_y \int_{-H}^{0} dz \int_{-H}^{z} dz'b' - \int_{-H}^{0} dz\,b\partial_y 0$$
$$+ \int_{-H}^{-H} dz\,b\partial_y(-H) = \partial_y \int_{-H}^{0} dz \int_{-H}^{z} dz'b'. \quad (A11)$$

Thus:

$$fM_x = -Hg\partial_y\eta + H\partial_y \int_{-H}^{0} b\,dz + \partial_y \int_{-H}^{0} z b\,dz + \rho_0^{-1}\tau_{0y}$$

$$(A12)$$

$$fM_y = Hg\partial_x\eta - H\partial_x \int_{-H}^{0} b\,dz - \partial_x \int_{-H}^{0} z b\,dz - \rho_0^{-1}\tau_{0x},$$

$$(A13)$$

where τ_{0x}, τ_{0y} are the zonal and meridional component of the surface wind-stress, respectively.

A further simplification can be made by applying again Leibnitz's rule on the second and third term of the r.h.s.:

$$H\partial_y \int_{-H}^{0} b\,dz = H \int_{-H}^{0} \partial_y b\,dz + Hb_{-H}\partial_y H \quad (A14)$$

$$\partial_y \int_{-H}^{0} z b\,dz = \int_{-H}^{0} z\partial_y b\,dz - Hb_{-H}\partial_y H, \quad (A15)$$

where b_{-H} is the buoyancy at the bottom of the ocean. Substituting into Eqs. A12 and A13, the last term on the r.h.s. cancels out, yielding

$$fM_x = -Hg\partial_y\eta + H \int_{-H}^{0} \partial_y b\,dz + \int_{-H}^{0} z\partial_y b\,dz + \rho_0^{-1}\tau_{0y}$$

$$(A16)$$

$$fM_y = Hg\partial_x\eta - H \int_{-H}^{0} \partial_x b\,dz - \int_{-H}^{0} z\partial_x b\,dz - \rho_0^{-1}\tau_{0x}. $$

$$(A17)$$

The vertically integrated Ekman, thermohaline and bottom transports are thus:

$$f[M_{xe}, M_{ye}] = \left[\rho_0^{-1}\tau_{0y}, -\rho_0^{-1}\tau_{0x} \right] \quad (A18)$$

$$f[M_{xt}, M_{yt}] = \left[\int_{-H}^{0} z\partial_y b\,dz, - \int_{-H}^{0} z\partial_x b\,dz \right] \quad (A19)$$

$$f[M_{xb}, M_{yb}]$$
$$= \left[-Hg\partial_y\eta + H \int_{-H}^{0} \partial_y b\,dz, Hg\partial_x\eta - H \int_{-H}^{0} \partial_x b\,dz \right],$$
$$(A20)$$

as discussed by Mellor et al. (1982). Equations A16 and A17, and their decomposition into Eqs. A18–A20 constitute our final equations.

Note that usually the surface elevation is unknown, which precludes calculating the transport directly from Eqs. A16 and A17. As explained by Mellor et al. (1982) this problem can be circumvented by rewriting these equations in terms of the potential energy at depth H $\rho_0\phi$ and the bottom pressure $\rho_0 P_b$:

$$\phi \equiv \int_{-H}^{0} z b\,dz \quad (A21)$$

$$P_b \equiv g\eta - \int_{-H}^{0} b\,dz. \quad (A22)$$

These are related to the second and third terms on the r.h.s. of Eqs. A16 and A17 in the following manner:

$$\partial_y\phi = \partial_y \int_{-H}^{0} z b\,dz = \int_{-H}^{0} z\partial_y b\,dz - Hb_{-H}\partial_y H; \quad (A23)$$

$$-H\partial_y P_b = -Hg\eta + \partial_y \int_{-H}^{0} b\,dz$$
$$= -Hg\eta + \int_{-H}^{0} \partial_y b\,dz + Hb_{-H}\partial_y H. \quad (A24)$$

Since the last term on the r.h.s. cancels out, Eqs. A16 and A17 can also be written as:

$$M_x = \frac{1}{f}\left\{-H\partial_y P_b + \partial_y \phi + \frac{\tau_{0y}}{\rho_0}\right\} \tag{A25}$$

$$M_y = \frac{1}{f}\left\{H\partial_x P_b - \partial_x \phi - \frac{\tau_{0x}}{\rho_0}\right\}. \tag{A26}$$

Cross-differentiating and adding up Eqs. A25 and A26 yields the equation for the advection of planetary potential vorticity, in which the bottom pressure term has been eliminated:

$$\mathbf{M} \cdot \nabla\left(\frac{f}{H}\right) = H^{-2}(\partial_y H \partial_x \phi - \partial_x H \partial_y \phi) + \partial_x\left(\frac{\tau_{0y}}{\rho_0 H}\right) - \partial_y\left(\frac{\tau_{0x}}{\rho_0 H}\right), \tag{A27}$$

which allows estimating the flow by evaluating the r.h.s. of Eq. A27; the reader is referred to Mellor et al. (1982) and Mellor (1996) for a more detailed explanation of the exact procedure. In our case, however, because we are handling model output, all quantities are available and the transport can be computed directly from Eqs. A16 and A17.

References

Böning C, Scheinert M, Dengg J, Biastoch A, Funk A (2006) Decadal variability of subpolar gyre transport and its reverberation in the North Atlantic overturning. Geophys Res Lett 33:L21S01

Born A, Levermann A, Mignot J (2009a) Sensitivity of the Atlantic circulation to a hydraulic overflow parameterization in a coarse resolution model. Ocean Modelling 27:132–140

Born A, Nisancioglu K, Braconnot P (2009b) Sea ice induced changes in ocean circulation during the Eemian. Climate Dynamics. doi: 10.1007/s00382-009-0709-2

Bryan F, Böning C, Holland W (1995) On the midlatitude circulation in a high-resolution model of the North Atlantic. J Phys Oceanogr 25(3):289–305

Crowley TJ, North GR (1991) Paleoclimatology. Oxford University Press, New York, p 349

Curry R, McCartney M, Joyce T (1998) Oceanic transport of subpolar climate signals to mid-depth subtropical waters. Nature 391:575–577

Eden C, Willebrand J (2001) Mechanism of interannual to decadal variability of the North Atlantic circulation. J Clim 14:2266–2280

Fichefet T, Maqueda MAM (1997) Sensitivity of a global sea ice model to the treatment of ice thermodynamics and dynamics. J Geophys Res 102:12609–12646

Fofonoff NP (1962) The Sea. In: Hill MN (ed) Dynamics of ocean currents, vol I. Interscience, New York

Ganachaud A, Wunsch C (2000) Improved estimates of global ocean circulation, heat transport and mixing from hydrographic data. Nature 48: 453–457

Ganopolski A, Rahmstorf S (2001) Rapid changes of glacial climate simulated in a coupled climate model. Nature 409:153–158

Greatbatch R, Fanning A, Goulding A, Levitus S (1991) A diagnosis of interpentadal circulation changes in the North Atlantic. J Geophys Res 96:22009–22023

Häkkinen S, Rhines PB (2004) Decline of subpolar North Atlantic circulation during the 1990s. Science 304:555–559

Hátún H, Sando A, Drange H, Hansen B, Valdimarsson H (2005) Influence of the Atlantic subpolar gyre on the thermohaline circulation. Science 309:1841–1844

Hewitt CD, Stouffer RJ, Broccoli AJ, Mitchell JFB, Valdes PJ (2003) The effect of ocean dynamics in a coupled GCM simulation of the Last Glacial Maximum. Clim Dyn 20:203–218

Kuhlbrodt T, Griesel A, Montoya M, Levermann A, Hofmann M, Rahmstorf S (2007) On the driving processes of the Atlantic meridional overturning circulation. Rev Geophys 45:RG2001

Levermann A, Born A (2007) Bistability of the subpolar gyre in a coarse resolution climate model. Geophys Res Lett 34:L24605

Mellor GL (1996) Introduction to physical oceanography. Princeton University

Mellor G, Mechoso C, Keto E (1982) A diagnostic calculation of the general circulation of the Atlantic Ocean. Deep Sea Res 29:1171–1192

Montoya M, Griesel A, Levermann A, Mignot J, Hofmann M, Ganopolski A, Rahmstorf S (2005) The Earth system model of intermediate complexity CLIMBER-3α. Part I: description and performance for present day conditions. Clim Dyn 25:237–263

Montoya M, Levermann A (2008) Surface wind-stress threshold for glacial atlantic overturning. Geophys Res Lett 35:L03608. doi: 10.1029/2007GL032,560

Myers P, Fanning A, Weaver A (1996) Jebar, bottom pressure torque, and gulf stream separation. J Phys Oceanogr 26:671–683

Otto-Bliesner B, Brady E, Tomas R, Levis S, Kothavala Z (2006) Last Glacial Maximum and Holocene climate in CCSM3. J Clim 19:2526–2544

Peltier WR (2004) Global glacial isostasy and the surface of the ice-age Earth: the ICE-5G(VM 2) model and GRACE. Annu Rev Earth Planet Sci 32(1):111–149

Penduff T, Barnier B, de Verdière AC (2000) Self-adapting open boundaries for a sigma coordinate model of the eastern North Atlantic. J Geophys Res 105:11279–11298

Petoukhov V, Ganopolski A, Brovkin V, Claussen M, Eliseev A, Kubatzki C, Rahmstorf S (2000) CLIMBER-2: a climate system model of intermediate complexity. Part I: model description and performance for present climate. Clim Dyn 16:1–17

Rahmstorf S (1996) On the freshwater forcing and transport of the Atlantic thermohaline circulation. Clim Dyn 12:799–811

Rahmstorf S (2002) Ocean circulation and climate during the past 120,000 years. Nature 419:207–214

Talley LD, Reid JL, Robbins PE (2003) Data-based meridional overturning streamfunctions for the global ocean. J Clim 16:3213–3226

Thornalley D, Elderfield H, McCave N (2009) Holocene Oscillations in the temperature and salinity of the surface subpolar North Atlantic. Nature 457:711–714

Toggweiler J, Russell J (2008) Ocean circulation in a warming climate. Nature 451:286-288

Toggweiler JR, Samuels B (1998) On the ocean's large scale circulation in the limit of no vertical mixing. J Phys Oceanogr 28:1832–1852

Treguier AM, Theetten S, Chassignet E, Penduff T, Smith R, Talley L, Beismann J, Böning C (2005) The North Atlantic subpolar gyre in four high-resolution models. J Clim 35:757–774

Trenberth K, Olson J, Large W (1989) A global ocean wind stress climatology based on ECMWF analyses. Tech. Rep. NCAR/TN-338+STR, National Center for Atmospheric Research, Boulder, Colorado, USA

Wijffels SE, Meyers G, Godfrey JS (2008) A 20-yr average of the Indonesian throughflow: regional currents and the interbasin exchange. J Phys Oceanogr 38:1965–1978

Wunsch C (1998) The work done by the wind on the oceanic general circulation. J Phys Oceanogr 28:2332–2340

Wunsch C, Ferrari R (2004) Vertical mixing, energy and the general circulation of the oceans. Annu Rev Fluid Mech 36:281–314

Zhang R (2008) Coherent surface-subsurface fingerprint of the Atlantic meridional overturning circulation. Geophys Res Lett 35:L20705